Research Article

Fuzhang Wang, Umar Nazir, Muhammad Sohail*, Essam R. El-Zahar, Choonkil Park*, and Phatiphat Thounthong

A Galerkin strategy for tri-hybridized mixture in ethylene glycol comprising variable diffusion and thermal conductivity using non-Fourier's theory

https://doi.org/10.1515/ntrev-2022-0050
received November 21, 2021; accepted January 13, 2022

Abstract: This research is conducted to investigate heat and mass transport past over a stretched surface having pores in a pseudo-plastic model. To study porosity effect, Darcy Forchheimer relation is used. Thermal and mass transport expressions are derived by engaging the double diffusion theories as extensively used by researchers proposed by Cattaneo and Christov. Furthermore, the thermal performance is studied by mixing the tri-hybrid nanoparticles in a pseudo-plastic material. The phenomenon of boundary layer is used to derive the complex model. The correlation for tri-hybrid nanoparticles is used to convert the model partial differential equations into ordinary differential equations (ODE) along with appropriate similarity transformation. The transfigured ODEs are coupled nonlinear in nature, and the exact solution is not possible. To approximate the solution numerically, finite element scheme (FES) is used and code is developed in MAPLE 18.0 for the graphical results, grid independent survey, and tabular results. The obtained results are compared with the published findings that confirm the accuracy and authenticity of the solution and engaged scheme. From the performed analysis, it is concluded that FES can be applied to complex engineering problems. Furthermore, it is monitored that nanoparticles are essential to boost the thermal performance and higher estimation of Schmidt number control the mass diffusion.

Keywords: Darcy's Forchheimer medium, variable diffusion and thermal conductivity, generalized diffusion models, grid independent investigation, finite element scheme

*** Corresponding author: Muhammad Sohail,** Department of Applied Mathematics and Statistics, Institute of Space Technology, P.O. Box 2750, Islamabad 44000, Pakistan, e-mail: muhammad_sohail111@yahoo.com
*** Corresponding author: Choonkil Park,** Research Institute for Natural Sciences, Hanyang University, Seoul 04763, Republic of Korea, e-mail: baak@hanyang.ac.kr
Fuzhang Wang: Department of Mathematics, Nanchang Institute of Technology, Nanchang 330044, China; College of Mathematics and Statistics, Xuzhou University of Technology, 221018 Xuzhou, China
Umar Nazir: Department of Applied Mathematics and Statistics, Institute of Space Technology, P.O. Box 2750, Islamabad 44000, Pakistan
Essam R. El-Zahar: Department of Mathematics, College of Science and Humanities in Al-Kharj, Prince Sattam Bin Abdulaziz University, P.O. Box 83, Al-Kharj 11942, Saudi Arabia; Department of Basic Engineering Science, Faculty of Engineering, Menoufia University, Shebin El-Kom 32511, Egypt
Phatiphat Thounthong: Renewable Energy Research Centre, Department of Teacher Training in Electrical Engineering, Faculty of Technical Education, King Mongkut's University of Technology North Bangkok, 1518 Pracharat 1 Road, Bangsue, Bangkok 10800, Thailand

1 Introduction

Fluid flows past over a stretched and rotated surfaces have gained much attention of the researchers due to their wider applications. Diffusion theories play a vital role to control heat and mass transportation in fluid flows. Researchers have much attraction to study physical problems discussing thermal transport. To keep thermal stability and maintain high thermal performance, mixing of nanoparticles is essential, and it boosts the heat transfer in fluid flows. Several models of nanofluids have been proposed and extensively used. Buongiorno's model discusses the involvement of Brownian motion and thermophoresis, whereas the single phase model contains the involvement of volume fraction and also researchers have addressed numerous relations that present the involvement of particles shapes. Several remarkable attempts have been made to discuss the utilization of nanoparticles in fluid flows. For instance, Koriko *et al.* [1] discussed the growth of energy transfer inserting nanoparticles along with bioconvection flow in the presence of magnetic field and gyrotactic microorganisms towards a vertical surface. Ali *et al.* [2] studied the role of hybrid nanoparticles in the energy transfer under the action of viscous dissipation.

Saleem and Heidarshenas [3] investigated the study of various nanoparticles in wavy wall in view of heat transfer phenomena. Pop *et al.* [4] discussed the role of magneto-hydrodynamic in stagnation point flow along with hybrid nanoparticles considering melting aspects. Tlili *et al.* [5] estimated features of nanoparticles in an unsteady flow using various shapes of nanoparticles considering Old-royd-B ferrofluid under the action of magnetic field. Qin [6] estimated the heat transfer features including the role of nanostructures in chamber. Nawaz *et al.* [7] discussed the comparative analysis among hybrid nanoparticles and nanoparticles into dust particles considering hyperbolic tangent liquid adopting the finite element approach. Nazir *et al.* [8] used the finite element approach to analyse comparative investigation between hybrid nanostructures and nanostructure in base liquid called ethylene glycol in Carreau Yasuda liquid. Nazir *et al.* [9] used non-Fourier's law in rheology of hyperbolic tangent liquid inserting vital impact of hybrid nanostructures towards a stretching surface. Nazir *et al.* [10] discussed the thermal character of hybrid nanostructures in hyperbolic tangent rheology in the base fluid (ethylene glycol) *via* finite element approach. Sheikholeslami and Farshad [11] concluded thermal aspects of the solar collector system inserting hybrid nanostructures. Swain *et al.* [12] used an exponentially surface to analyse a role of hybrid nanostructures in the presence of chemical reaction *via* slip conditions. Faraji *et al.* [13] developed a model related to phase change liquid in view of hybrid nanomaterials along with heat source in a rectangular enclosure. Abdelmalek *et al.* [14] investigated an inclination into heat energy using nanoparticles and hybrid nanostructures in view of base fluid in wedge. They have used finite element scheme (FES) to know comparison among hybrid nanostructures and nanostructures including chemical reaction into solute particles. Nawaz *et al.* [15] analysed rheology of power law liquid into solute particles and thermal energy inserting an impact of hybrid nanoparticles over a heated surface *via* finite element approach. Latocha *et al.* [16] estimated prediction of hydroxyapatite in nanoparticles towards 3D-printed reactors. Haider *et al.* [17] discussed the role of hybrid nanoparticles in Williamson liquid using heat flux model. They adopted heated surface to captures comparison performance of hybrid nanoparticles and hybrid nanoparticles in ethylene glycol. Nazir *et al.* [18] discussed features of thermal energy using nanoparticles towards a surface in Casson liquid. Dadheech *et al.* [19] analysed the comparison of heat energy performance among SiO_2-MoS_2 hybrid nanofluid and nanofluid (MoS_2) in ethylene glycol under the presence of magnetic field. Shafiq *et al.* [20] discussed the heat energy features in Walters' B nanofluid over a Riga plate *via* statistical approach. Marzougui *et al.* [21] used the lid-driven cavity to capture the impacts of entropy generation and thermal transfer in the attendance of non-variable magnetic field. Pushpa *et al.* [22] captured flow and convective thermal transfer inserting nanoparticles in thin baffle. Dhif *et al.* [23] studied the performance of hybrid nanoparticles in a solar collector system. Abdelsalam *et al.* [24] discussed the study related to Rabinowitsch suspension in the presence of leveraging elasticity in a wavelike conduit. Abdelsalam *et al.* [25] conducted results of swimming sperms in the presence of electro-magnetically using a wavelike conduit. Raza *et al.* [26] adopted curved surface to achieve consequences in Williamson liquid under thermal radiation. Eldesoky *et al.* [27] integrated thermal features into conjunction along with slip conditions in view of peristaltic motion using a catheterized pipe. Bhatti and Abdelsalam [28] captured peristaltic motion adding hybrid nanoparticles along with magnetic field. Elkoumy *et al.* [29] performed the role of Maxwell liquid in terms of peristaltic motion inserting magnetic field and Hall force. Bhatti *et al.* [30] simulated the heat transfer based on intra-uterine motion in channel. Some important contributions covering the modelling aspects are reported in earlier studies [31–36].

Current model is developed using the rheology of pseudo-plastic material along with the presence of tri-hybrid nanoparticles. The theories regarding non-Fourier's and Darcy's Forchheimer within heat generation and chemical reaction are investigated. FES is considered to find numerical simulations. Investigations regarding current model is not achieved yet.

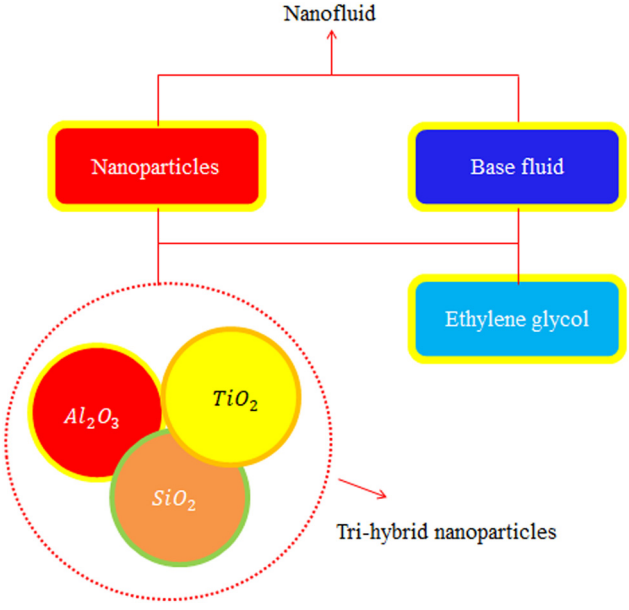

Figure 1: Prepared approach regarding mixtures of ternary hybrid nanoparticles.

- Section 1 presents literature survey;
- Section 2 presents modelling;
- Section 3 contains methodology procedure and mesh-free investigations; and
- Section 4 reports detailed discussion and description of obtained solution against numerous involved parameters, and Section 5 lists important findings. Developing approach of tri-hybrid nanoparticles is shown in Figure 1.

2 Flow analysis of tri-hybrid nanoparticles

The flow of tri-hybrid nanoparticles in pseudo-plastic liquid towards the heated surface is addressed. Solute particles and heat energy of particles are analysed considering the theory of Cattaneo–Christov model (CCM). Processes of chemical reaction and heat generation are implemented in the presence of CCM. The concept of Forchheimer porous is modelled in the momentum equation. Layers associated with momentum and thermal are generated because of stretching of plate. Composite relation among nanofluid, nanoparticles, hybrid nanomaterials, and tri-hybrid nanoparticles is considered in equations (12)–(14). Physical configuration of current model is captured in Figure 2 (Table 1).

System of formulated partial differential equations [33–35] is as follows:

$$\frac{\partial \dot{U}}{\partial x} + \frac{\partial \dot{V}}{\partial y} = 0, \tag{1}$$

$$\dot{U}\frac{\partial \dot{U}}{\partial x} + \dot{V}\frac{\partial \dot{U}}{\partial y} = \nu_{\text{Thnf}}\frac{\partial}{\partial y}\left(\left|\frac{\partial \dot{U}}{\partial y}\right|^{m-1}\frac{\partial \dot{U}}{\partial y}\right) - \frac{\nu_{\text{Thnf}}}{k^{s}}F_{\text{D}}\dot{U} - \frac{F_{\text{D}}}{(k^{s})^{\frac{1}{2}}}\dot{U}^{2}, \tag{2}$$

$$\dot{U}\frac{\partial T}{\partial x} + \dot{V}\frac{\partial T}{\partial y} + \lambda_{t}\left(\begin{array}{c}\dot{U}\dfrac{\partial \dot{U}}{\partial x}\dfrac{\partial T}{\partial x} + \dot{V}\dfrac{\partial \dot{V}}{\partial y}\dfrac{\partial T}{\partial y} + \dot{U}\dfrac{\partial \dot{V}}{\partial x}\dfrac{\partial T}{\partial y} + 2\dot{U}\dot{V}\dfrac{\partial^{2}T}{\partial x\partial y}\\ \dot{U}^{2}\dfrac{\partial^{2}T}{\partial x^{2}} + \dot{V}^{2}\dfrac{\partial^{2}T}{\partial y^{2}} - \dfrac{Q}{(\rho C_{\text{p}})_{\text{hnf}}}\left(\dot{U}\dfrac{\partial T}{\partial x} + \dot{V}\dfrac{\partial T}{\partial y}\right)\\ +\dot{V}\dfrac{\partial \dot{U}}{\partial y}\dfrac{\partial T}{\partial x}\end{array}\right) = \frac{1}{(\rho C_{\text{p}})_{\text{hnf}}}\frac{\partial}{\partial y}\left(k^{T}_{\text{Thnf}}\frac{\partial T}{\partial y}\right) + \frac{Q}{(\rho C_{\text{p}})_{\text{hnf}}}(T - T_{\infty}), \tag{3}$$

$$\dot{U}\frac{\partial C}{\partial x} + \dot{V}\frac{\partial C}{\partial y} + \lambda_{\text{c}}\left(\begin{array}{c}\dot{U}\dfrac{\partial \dot{U}}{\partial x}\dfrac{\partial C}{\partial x} + \dot{V}\dfrac{\partial \dot{V}}{\partial y}\dfrac{\partial C}{\partial y} + \dot{U}\dfrac{\partial \dot{V}}{\partial x}\dfrac{\partial C}{\partial y} + 2\dot{U}\dot{V}\dfrac{\partial^{2}C}{\partial x\partial y}\\ \dot{U}^{2}\dfrac{\partial^{2}C}{\partial x^{2}} + \dot{V}^{2}\dfrac{\partial^{2}C}{\partial y^{2}} - K_{\text{a}}\left(\dot{U}\dfrac{\partial C}{\partial x} + \dot{V}\dfrac{\partial C}{\partial y}\right)\\ +\dot{V}\dfrac{\partial \dot{U}}{\partial y}\dfrac{\partial C}{\partial x}\end{array}\right) = \frac{\partial}{\partial y}\left(D^{C}_{\text{Thnf}}\frac{\partial C}{\partial y}\right) + K_{\text{a}}(C - C_{\infty}). \tag{4}$$

Where heat generation is Q, temperature is T, thermal conductivity is k, fluid density is ρ, velocities are $(\dot{U},\ \dot{V})$, time relaxation is λ_{t}, specific heat capacitance is denoted by C_{P}, kinematic viscosity is ν, power law number is m, space coordinates are y, x, tri-hybrid nanoparticles are represented by Thnf, ambient temperature is T_{∞}, permeability within porous medium is $k_{\star}$, inertia coefficient in term of porous medium is F_{D}, C is concentration, ambient concentration is C_{∞}, chemical reaction K_{a}, and mass diffusion is D. No-slip theory is used to generate boundary conditions (BCs) and required conditions are as follows:

$$\begin{aligned}&\dot{U} = u_{\text{w}},\ \dot{V} = -v_{\text{w}}, C = C_{\text{w}},\ T = T_{\text{w}} \text{ at } y = 0,\\ &\dot{U} \to u_{\infty},\ C \to C_{\infty},\ T \to T_{\infty} \text{ when } y \to \infty.\end{aligned} \tag{5}$$

Transformations of model are as follows:

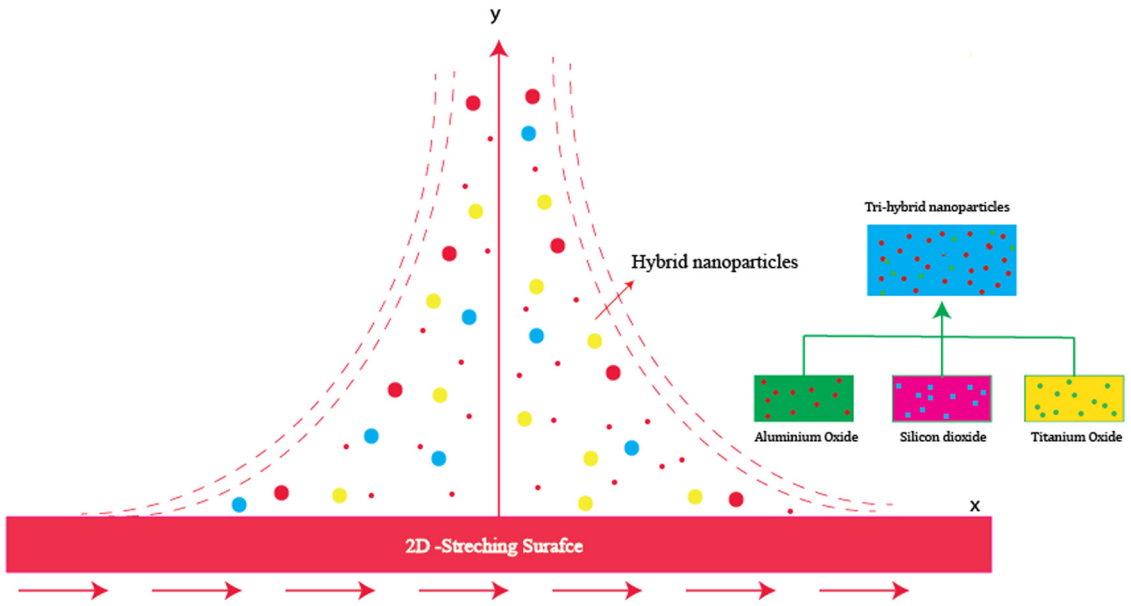

Figure 2: Geometry of the developed model.

$$\theta = \frac{T - T_\infty}{T_w - T_\infty}, \theta = \frac{C - C_\infty}{C_w - C_\infty} \xi = y\left(\frac{U^{2-m}}{x\nu_f}\right)^{\frac{1}{m+1}}, \quad (6)$$

Variable thermal conductivity and variable mass diffusion in view of tri-hybrid nanoparticles [36] are defined as follows:

$$k^t_{\text{Thnf}} = k_{\text{Thnf}}\left[1 + \varepsilon_1\left(\frac{T - T_\infty}{T_w - T_\infty}\right)\right], \quad (7)$$

$$D^c_{\text{Thnf}} = D_{\text{Thnf}}\left[1 + \varepsilon_2\left(\frac{T - T_\infty}{T_w - T_\infty}\right)\right]. \quad (8)$$

Transformations deliver system of ODEs and nonlinear ODEs are as follows:

$$(|F''|^{m-1}F'')' + \frac{1}{m+1}F''F - \varepsilon F' - \frac{\nu_f}{\nu_{\text{Thnf}}}F_R(F'^2) = 0, \quad (9)$$

$$(1 + \varepsilon_1\theta)\theta'' + \varepsilon_1(\theta')^2 + \frac{\text{Pr}}{m+1}F\theta' - \frac{k_f(\rho C_p)_{\text{hnf}}}{k_{\text{hnf}}(\rho C_p)_f}\text{Pr}\Omega_a [FF'\theta' + F^2\theta'' + H_hF\theta'] + \frac{k_f}{k_{\text{hnf}}}H_h\text{Pr}\theta = 0, \quad (10)$$

$$(1 + \varepsilon_2\phi)\phi'' + \varepsilon_2\theta'\phi' - \frac{(1-\phi_2)^{-2.5}\text{Sc}}{(1-\phi_1)^{2.5}(1-\phi_3)^{2.5}}\text{Pr}\Omega_c \times [FF'\phi' + F^2\phi'' + K_cF\phi'] - \frac{(1-\phi_2)^{-2.5}\text{Sc}}{(1-\phi_1)^{2.5}(1-\phi_3)^{2.5}}K_c\phi + \frac{(1-\phi_2)^{-2.5}\text{Sc}}{(1-\phi_3)^{2.5}m + 1(1-\phi_1)^{2.5}}F\phi' = 0. \quad (11)$$

Properties associated with thermal for correlations among tri-hybrid nanoparticles are as follows:

$$\rho_{\text{Thnf}} = (1-\varphi_1)\{(1-\varphi_2)[(1-\varphi_3)\rho_f + \varphi_3\rho_3] + \varphi_2\rho_2\} + \varphi_1\rho_1, \quad (12)$$

$$\frac{\mu_f}{(1-\varphi_3)^{2.5}(1-\varphi_2)^{2.5}(1-\varphi_1)^{2.5}}, \quad \frac{K_{\text{hnf}}}{K_{\text{nf}}} = \frac{K_2 + 2K_{\text{nf}} - 2\varphi_1(K_{\text{nf}} - K_2)}{K_2 + 2K_{\text{nf}} + \varphi_2(K_{\text{nf}} - K_2)}, \quad (13)$$

$$\frac{K_{\text{Thnf}}}{K_{\text{hnf}}} = \frac{K_1 + 2K_{\text{hnf}} - 2\varphi_1(K_{\text{hnf}} - K_1)}{K_1 + 2K_{\text{hnf}} + \varphi_1(K_{\text{hnf}} - K_1)}, \quad \frac{K_{\text{nf}}}{K_f} = \frac{K_3 + 2K_f - 2\varphi_3(K_f - K_3)}{K_3 + 2K_f + \varphi_3(K_f - K_3)}, \quad (14)$$

Table 1: Thermal properties of ethylene glycol, silicon dioxide, aluminium oxide, and titanium dioxide-related nanoparticles in EG

	K (thermal conductivity)	σ (electrical conductivity)	ρ (density)
$C_2H_6O_2$	0.253	4.3×10^{-5}	1113.5
Al_2O_3	32.9	5.96×10^{7}	6,310
TiO_2	8.953	2.4×10^{6}	4,250
SiO_2	1.4013	3.5×10^{6}	2,270

$$\frac{\sigma_{\mathrm{Tnf}}}{\sigma_{\mathrm{hnf}}} = \frac{\sigma_1(1+2\varphi_1) - \varphi_{\mathrm{hnf}}(1-2\varphi_1)}{\sigma_1(1-\varphi_1) + \sigma_{\mathrm{hnf}}(1+\varphi_1)}, \quad \frac{\sigma_{\mathrm{hnf}}}{\sigma_{\mathrm{nf}}} = \frac{\sigma_2(1+2\varphi_2) + \varphi_{\mathrm{nf}}(1-2\varphi_2)}{\sigma_2(1-\varphi_2) + \sigma_{\mathrm{nf}}(1+\varphi_2)}, \tag{15}$$

$$\frac{\sigma_{\mathrm{nf}}}{\sigma_{\mathrm{f}}} = \frac{\sigma_3(1+2\varphi_3) + \varphi_{\mathrm{f}}(1-2\varphi_3)}{\sigma_3(1-\varphi_3) + \sigma_{\mathrm{f}}(1+\varphi_3)}. \tag{16}$$

The formulated skin friction coefficient is defined as follows:

$$C_{\mathrm{f}} = \frac{2(\tau_{\mathrm{w}})}{U^2\rho_{\mathrm{f}}}, \tag{17}$$

$$(\mathrm{Re})^{\frac{1}{m+1}} C_{\mathrm{f}} = -\frac{(1-\varphi_2)^{-2.5}}{(1-\varphi_1)^{2.5}(1-\varphi_3)^{2.5}}[F''(0)|F''(0)|^{m-1}]. \tag{18}$$

The temperature gradient is modelled as follows:

$$\mathrm{Nu} = \frac{xQ_{\mathrm{w}}}{(T_{\mathrm{w}} - T_\infty)k_{\mathrm{f}}}, \quad (\mathrm{Re})^{\frac{-1}{m+1}}\ \mathrm{Nu} = -\frac{k_{\mathrm{Thnf}}}{k_{\mathrm{f}}}\theta'(0). \tag{19}$$

The rate of mass diffusion is as follows:

$$\mathrm{Sc} = \frac{xM_{\mathrm{w}}}{(C_{\mathrm{w}} - C_\infty)D_{\mathrm{f}}}, \quad (\mathrm{Re})^{\frac{-1}{m+1}}\mathrm{Sc} = -\frac{(1-\phi_2)^{-2.5}}{(1-\phi_1)^{2.5}(1-\phi_3)^{2.5}}\phi'(0). \tag{20}$$

Reynolds number is $\mathrm{Re} = \left(\frac{x^m U^{2-m}}{\nu_{\mathrm{f}}}\right)$.

3 Numerical scheme

FES is utilized to simulate numerical results. FES is very capable of simulating CFD problems. Detail steps are described below.

Step I: Equations (6) and (7) within BCs are called the strong form. It is noticed that collecting all terms of equations (6) and (7) on one side and integrating it over each elements of domain are residuals. Such procedure is known as weighted (residual method) for the development of weak forms. The residuals are as follows:

$$\int_{\eta_{e+1}}^{\eta_e} Q_1(F' - S)\mathrm{d}\xi = 0, \tag{21}$$

$$\int_{\eta_e}^{\eta_{e+1}} Q_2\left[(|F''|^{m-1}F'')' + \frac{1}{m+1}F''F - \varepsilon F' - \frac{\nu_{\mathrm{f}}}{\nu_{\mathrm{Thnf}}}F_{\mathrm{R}}(F'^2)\right]\mathrm{d}\xi = 0, \tag{22}$$

$$\int_{\eta_e}^{\eta_{e+1}} Q_3\left[(1+\varepsilon_1\theta)\theta'' + \varepsilon_1(\theta')^2 + \frac{\mathrm{Pr}}{m+1}F\theta' + \frac{k_{\mathrm{f}}}{k_{\mathrm{hnf}}}H_{\mathrm{h}}\mathrm{Pr}\theta - \frac{k_{\mathrm{f}}(\rho C_{\mathrm{p}})_{\mathrm{hnf}}}{k_{\mathrm{hnf}}(\rho C_{\mathrm{p}})_{\mathrm{f}}}\mathrm{Pr}\Omega_{\mathrm{a}}[FF'\theta' + F^2\theta'' + H_{\mathrm{h}}F\theta']\right]\mathrm{d}\xi = 0, \tag{23}$$

$$\int_{\eta_e}^{\eta_{e+1}} Q_4\left[-\frac{(1-\phi_2)^{-2.5}\mathrm{Sc}}{(1-\phi_1)^{2.5}(1-\phi_3)^{2.5}}K_{\mathrm{c}}\phi + \frac{(1-\phi_2)^{-2.5}\mathrm{Sc}}{(1-\phi_3)^{2.5}m+1(1-\phi_1)^{2.5}}F\phi' \right.$$
$$\left. (1+\epsilon_2\phi)\phi'' + \varepsilon_2\theta'\phi' - \frac{(1-\phi_2)^{-2.5}\mathrm{Sc}}{(1-\phi_1)^{2.5}(1-\phi_3)^{2.5}}\mathrm{Pr}\Omega_{\mathrm{c}}[FF'\phi' + F^2\phi'' + K_{\mathrm{c}}F\phi']\right]\mathrm{d}\xi = 0. \tag{24}$$

Here, Q_1, Q_2, Q_3, and Q_4 are named as weight functions. The shape functions are as follows:

$$\pi_i = (-1)^{i-1}\left(\frac{-\xi + \xi_{i-1}}{-\xi_i + \xi_{i+1}}\right),\ i = 1,\ 2. \tag{25}$$

Step II: An approach associated with Galerkin finite element is imposed to obtain weak form in view of shape functions.

Step III: The assembly approach is utilized for the development of stiffness element, whereas assembly approach is performed *via* assembly procedure of FEA. Stiffness elements are as follows:

$$K_{ij}^{11} = \int_{\eta_e}^{\eta_{e+1}}\left(\frac{\mathrm{d}\pi_j}{\mathrm{d}\eta}\pi_i\right)\mathrm{d}\xi,\ K_{ij}^{12} = 0,\ K_{ij}^{14} = 0,\ K_{ij}^{13} = 0,\ B_i^1 = 0, \tag{26}$$

$$K_{ij}^{22} = \int_{\eta_e}^{\eta_{e+1}}\left[-|\overline{S}'|^{m-1}\frac{\mathrm{d}\pi_i}{\mathrm{d}\eta}\frac{\mathrm{d}\pi_j}{\mathrm{d}\eta} + |\overline{S}'|^{m-1}\frac{\mathrm{d}\pi_i}{\mathrm{d}\eta}\frac{\mathrm{d}\pi_j}{\mathrm{d}\eta} + \frac{1}{m+1}\bar{F}\pi_i\frac{\mathrm{d}\pi_j}{\mathrm{d}\eta} - \varepsilon\pi_i\frac{\mathrm{d}\pi_j}{\mathrm{d}\eta} - \frac{\nu_{\mathrm{f}}}{\nu_{\mathrm{Thnf}}}F_{\mathrm{R}}(\bar{S})\pi_i\pi_j\right]\mathrm{d}\xi, \tag{27}$$

$$K_{ij}^{21} = 0,\ K_{ij}^{23} = 0,\ K_{ij}^{24} = 0, B_i^2 = 0, \tag{28}$$

$$K_{ij}^{33} = \int_{\eta_e}^{\eta_{e+1}} \left[\begin{array}{c} -(1+\varepsilon_1\bar{\theta})\frac{d\pi_i}{d\eta}\frac{d\pi_j}{d\eta} + \frac{\Pr}{m+1}\bar{F}\pi_i\frac{d\pi_j}{d\eta} - \frac{k_f(\rho C_p)_{hnf}}{k_{hnf}(\rho C_p)_f}\Pr\Omega_a\bar{F}\bar{S}\pi_i\frac{d\pi_j}{d\eta} \\ + \frac{k_f(\rho C_p)_{hnf}}{k_{hnf}(\rho C_p)_f}\Pr\Omega_a\bar{F}^2\frac{d\pi_i}{d\eta}\frac{d\pi_j}{d\eta} - \frac{k_f(\rho C_p)_{hnf}}{k_{hnf}(\rho C_p)_f}\Pr\Omega_a H_h\bar{F}\pi_i\frac{d\pi_j}{d\eta} + \frac{k_f}{k_{hnf}}H_h\Pr\pi_i\pi_j \end{array} \right] d\xi, \tag{29}$$

$$\begin{gathered} K_{ij}^{31} = 0,\ K_{ij}^{32} = 0,\ K_{ij}^{34} = 0, B_i^3 = 0,\ K_{ij}^{41} = 0, \\ K_{ij}^{42} = 0,\ K_{ij}^{43}, B_i^4 = 0, \end{gathered} \tag{30}$$

$$\int_{\eta_e}^{\eta_{e+1}} \left[\begin{array}{c} -\frac{(1-\phi_2)^{-2.5}\mathrm{Sc}}{(1-\phi_1)^{2.5}(1-\phi_3)^{2.5}}K_c\pi_i\pi_j + \frac{(1-\phi_2)^{-2.5}\mathrm{Sc}}{(1-\phi_3)^{2.5}m+1(1-\phi_1)^{2.5}}\bar{F}\pi_i\frac{d\pi_j}{d\eta} \\ (1+\varepsilon_2\bar{\phi})^1\frac{d\pi_i}{d\eta}\frac{d\pi_j}{d\eta} + \varepsilon_2\overline{\phi'}\pi_i\frac{d\pi_j}{d\eta} - \frac{(1-\phi_2)^{-2.5}\mathrm{Sc}}{(1-\phi_1)^{2.5}(1-\phi_3)^{2.5}}\Pr\Omega_c\left(\bar{F}\bar{S}\pi_i\frac{d\pi_j}{d\eta}\right) \\ -\frac{(1-\phi_2)^{-2.5}\mathrm{Sc}}{(1-\phi_1)^{2.5}(1-\phi_3)^{2.5}}\left(\Pr\Omega_c K_c\bar{F}\phi'\pi_i\frac{d\pi_j}{d\eta} + \overline{F^2}\frac{d\pi_i}{d\eta}\frac{d\pi_j}{d\eta}\right) \end{array} \right] d\xi. \tag{31}$$

Step IV: Picard linearization approach provides the transformed algebraic system (linear equations).

Step V: Finally, system of linear algebraic equations is numerically solved within the computational tolerance (10^{-5}). The stopping condition is listed below.

$$\left| \frac{\delta_{i+1} - \delta_i}{\delta^i} \right| < 10^{-5}. \tag{32}$$

Step VI: Table 2 demonstrates study of mesh-free.

Step VII: A total of 300 elements are required to obtain convergence analysis. The programming of finite element method is generated using software related to MAPLE 18.

3.1 Validation of results

The comparison among present analysis and published results [33–35] are derived in Table 3. It is noticed that the present problem is reduced into published problems [33–35] by considering $\varphi_a = \varphi_b = \varphi_c = 0$, $F_r = \varepsilon = 0$. A good agreement between the results of the present problem and published works is noticed.

4 Graphical discussion and outcomes

Characteristics related to solute and thermal are established inserting comprehensive role of tri-hybrid nanoparticles *via* Darcy's Forchheimer law. Cattaneo–Christov law is used along with the dual role of thermal energy based on phenomena generation and absorption of heat energy. Diffusion of mass species is manufacturing in the presence non-Fourier's theory. Base fluid (ethylene glycol) is considered along with pseudo-plastic liquid. A strong approach is called finite element method to visualize graphical impacts of various parameters on concentration, velocity, and temperature profiles. Further, codding of finite element approach is designed by MAPLE 18 software. Current code is developed to simulate complex ODEs along with boundary conditions. Detail outcomes regarding the measurement of velocity, concentration, and thermal energy are mentioned below.

4.1 Analysis of velocity curves against physical parameters

Motion into nanoparticles, hybrid nanoparticles, and tri-hybrid nanoparticles are measured with respect to variation in power law number (m), Darcy's number (ε), and Forchheimer number (F_r). Figure 3a–c is prepared for the measurement of the velocity distribution *versus* m, ε, and F_r. Figure 3a prescribes the motion into nanoparticles *versus* distribution in ε. It is noticed that the presentation of ε happened because of pores at the surface. The flow of nanoparticles, ternary hybrid nanoparticles, and hybrid nanoparticles is declined over the surface. Momentum layers are decreased when ε is enhanced. Physically, higher values of ε produce frictional force into fluid

Table 2: Mesh-free study for temperature gradient, concentration gradient, and Sherwood number *via* 300 elements

Number of elements	$F'\left(\frac{\xi_{max}}{2}\right)$	$\theta\left(\frac{\xi_{max}}{2}\right)$	$\varphi\left(\frac{\xi_{max}}{2}\right)$
30	0.006299584904	0.5916150941	0.4046811155
60	0.004773218163	0.5635673948	0.6701679329
90	0.004333296367	0.5530486985	0.3494690039
120	0.004125211694	0.5475247702	0.3450328235
150	0.004004033797	0.5441183135	0.3440517986
180	0.003924751415	0.5418082729	0.3448555416
210	0.003868847656	0.5401363276	0.3467001955
240	0.003827313579	0.5388730488	0.3492091727
270	0.003795243660	0.5378847796	0.3522432276
300	0.003769731588	0.5370874271	0.3556147229

particles. Hence, the frictional force makes a reduction into motion among fluid layers. Hence, inverse proportional relation is existed among flow and ε. Impact of F_r on velocity curves is measured by Figure 3b, inserting the role of ternary hybrid nanoparticles. Appearance of F_r is model out due to impact of Darcy's Forchheimer law. A declination role into motion of particles is investigated when F_r is enhanced. Layers associated with the momentum boundary are investigated decreasing function against impact of F_r model related to Darcy–Forchheimer is based on Darcian motion into fluid particles. Mathematically, it appeared as a velocity squared in motion equations. A retardation motion is developed due to appearance of Forchheimer. Momentum layers have a decreasing function *versus* impact of F_r. Hence, fluid is termed as thick when F_r is increased. An effect of m on velocity curves is established in Figure 3c. It is estimated that the description of m is modelled out due to inserting impact of pseudo-plastic liquid. Moreover, the category of shear thinning, shear thickening, and Newtonian liquid is based on values m. For $m < 1$, fluid appeared as shear thickening among fluid particles. It is noticed that layers along with momentum layers are declined when m is increased.

Table 3: Validation of numerical results for skin friction coefficient

Skin friction coefficient		Present work skin friction coefficient
Sakiadis [33]	−0.44375	−0.446169
Fox *et al.* [34]	−0.4437	−0.442930
Chen [35]	−0.4438	−0.443731

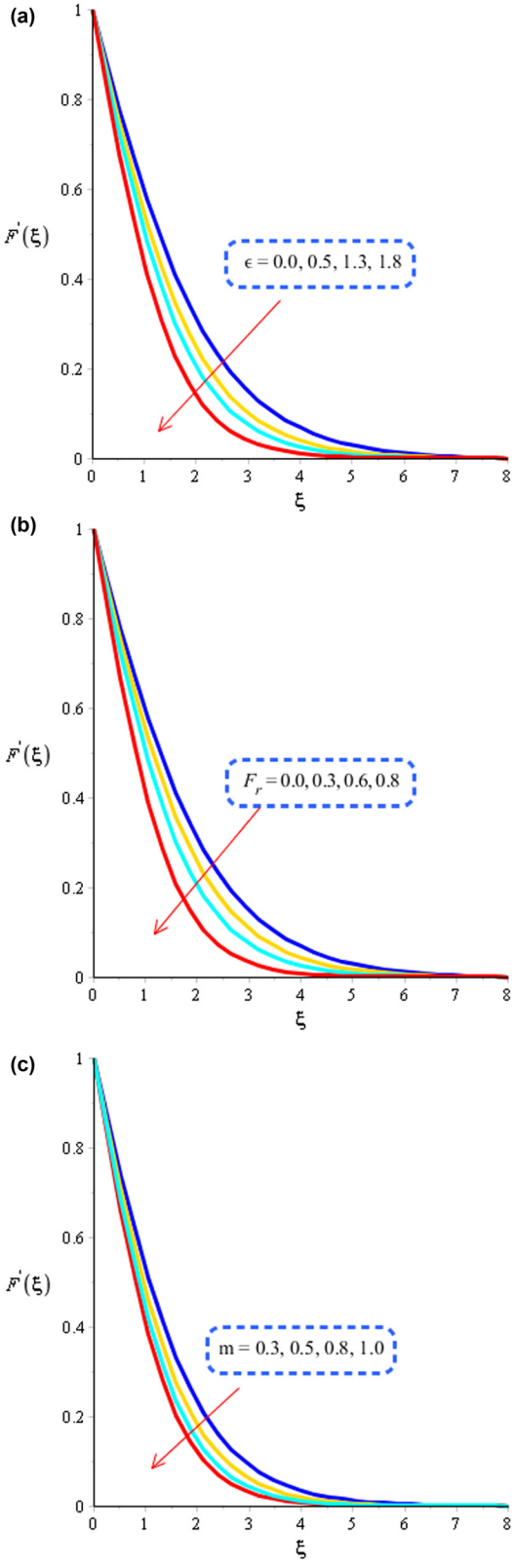

Figure 3: (a) Role of ε on velocity curves. (b) Role of F_r on velocity curves. (c) Role of m on velocity curves.

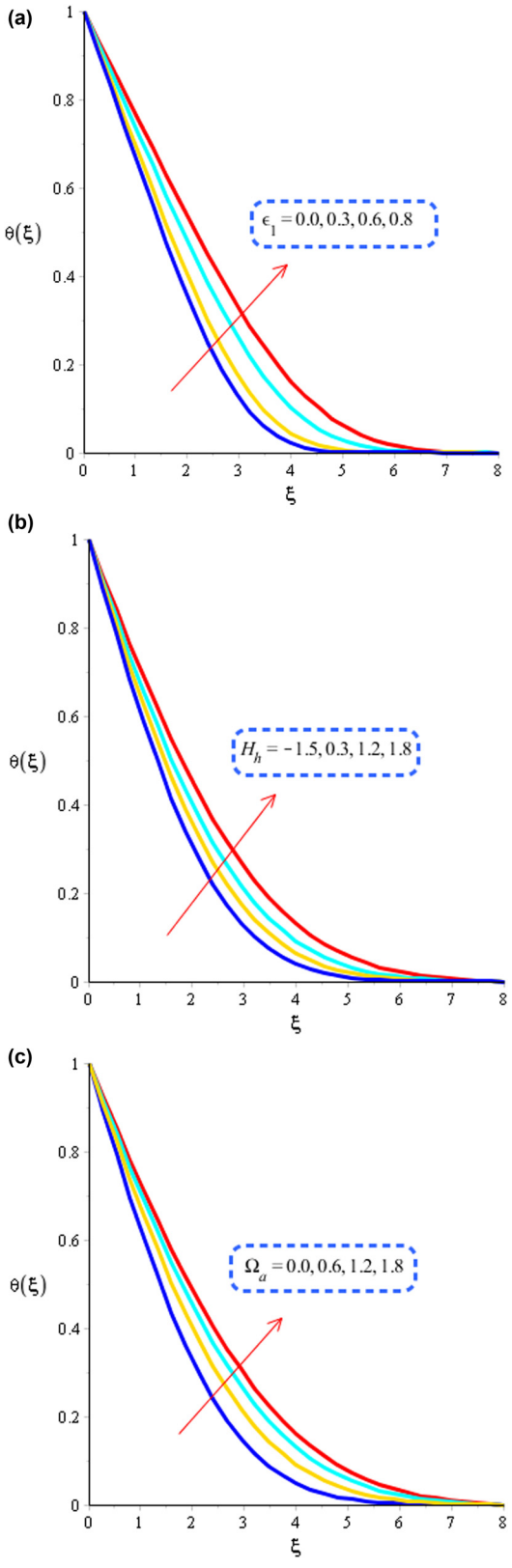

Figure 4: (a) Role of ε_1 on temperature curves. (b) Role of H_h on temperature curves. (c) Role of Ω_a on temperature curves.

4.2 Analysis of temperature curves against physical parameters

Thermal aspects including ternary hybrid nanoparticles are observed against variation in H_h, ε_1, and Ω_a. These thermal aspects are measured with respect to change in H_h, ε_1, and Ω_a by Figure 4a–c. The impact of variable thermal conductivity (ε_1) on temperature curves is examined by Figure 4a. It is noticed that thermal energy of particles is boosted when ε_1 is increased. The parameter related to ε_1 is produced because of variable thermal conductivity. Mathematically, ε_1 has a relationship related to direct proportional temperature. Hence, an increment into thermal energy is based on distribution in ε_1. Moreover, layers of thermal at boundary are increased *versus* higher values of ε_1. Physically, ε_1 has a directly proportional relation *versus* temperature difference. Hence, an increment in $\varepsilon_1$results in a significant ability of thermal energy to conduct more heat energy into fluid particles is observed. The ability to conduct temperature into hybrid and nanoparticles is also increased when ε_1 is increased. Figure 4b demonstrates influence of H_h on temperature curves. Dual role of heat energy is visualized on aspects of thermal energy while negative values of H_h are due to the role of heat absorption and positive values of H_h are due to the role of heat energy generation. Production into heat energy of particles is inclined into nanoparticles and tri-hybrid nanoparticles based on variation in H_h. Mathematically, H_h appeared in energy equation, which is a product of temperature difference. Basically, it occurred because of an external heat source. Thermal energy is boosted when an external heat source is placed at the wall. Boundary layers based on the thermal impact are increasing behaviour. This increasing effect of thermal energy is produced due to applying an external source of heat energy, which is placed at the wall of surface. Hence, the heat energy is established according to values of H_h. The prediction of heat energy against distribution in Ω_a is addressed by Figure 4c. Argumentation into heat energy is measured when Ω_a is increased. The parameter is called Ω_a is made because of non-Fourier's theory. Non-Fourier's theory is implemented in current analysis. Hence, heat energy is boosted when Ω_a is increased. An increasing function is investigated among Ω_a and thermal layers. Moreover, fluid particles take more time to restore more heat energy when Ω_a is increased. The layers associated within thermal are increasing inserting higher values of Ω_a. Figure 5 is observed as a vital impact on comparison of tri-hybrid nanoparticles, nanoparticles,

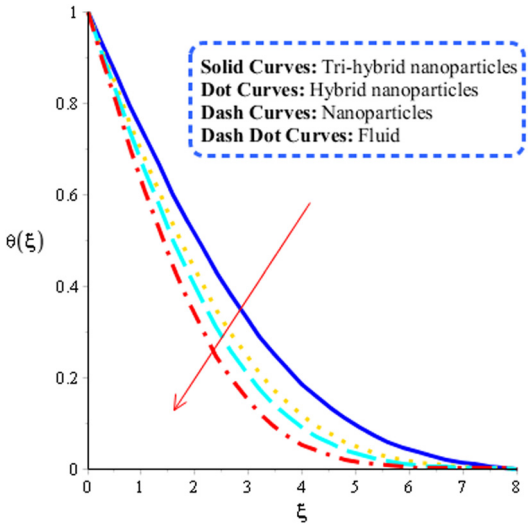

Figure 5: Comparison study among fluid, nanoparticles, hybrid nanoparticles and tri-hybrid nanoparticles.

and fluid and hybrid nanoparticles on the thermal performance. It is examined that a significant performance of ternary hybrid nanoparticles is addressed on the thermal performance. Maximum production of thermal energy is produced for tri-hybrid nanoparticles rather than production into thermal energy of hybrid nanoparticles, fluid and hybrid nanoparticles.

4.3 Analysis of concentration curves against physical parameters

Diffusion of solute particles is observed *versus* impacts of K_c, Ω_c, Sc, and ε_2 considering Figure 6a–d. Figure 6a illustrates that the variation into thermal energy is verified against chemical reaction number (K_c). In this figure,

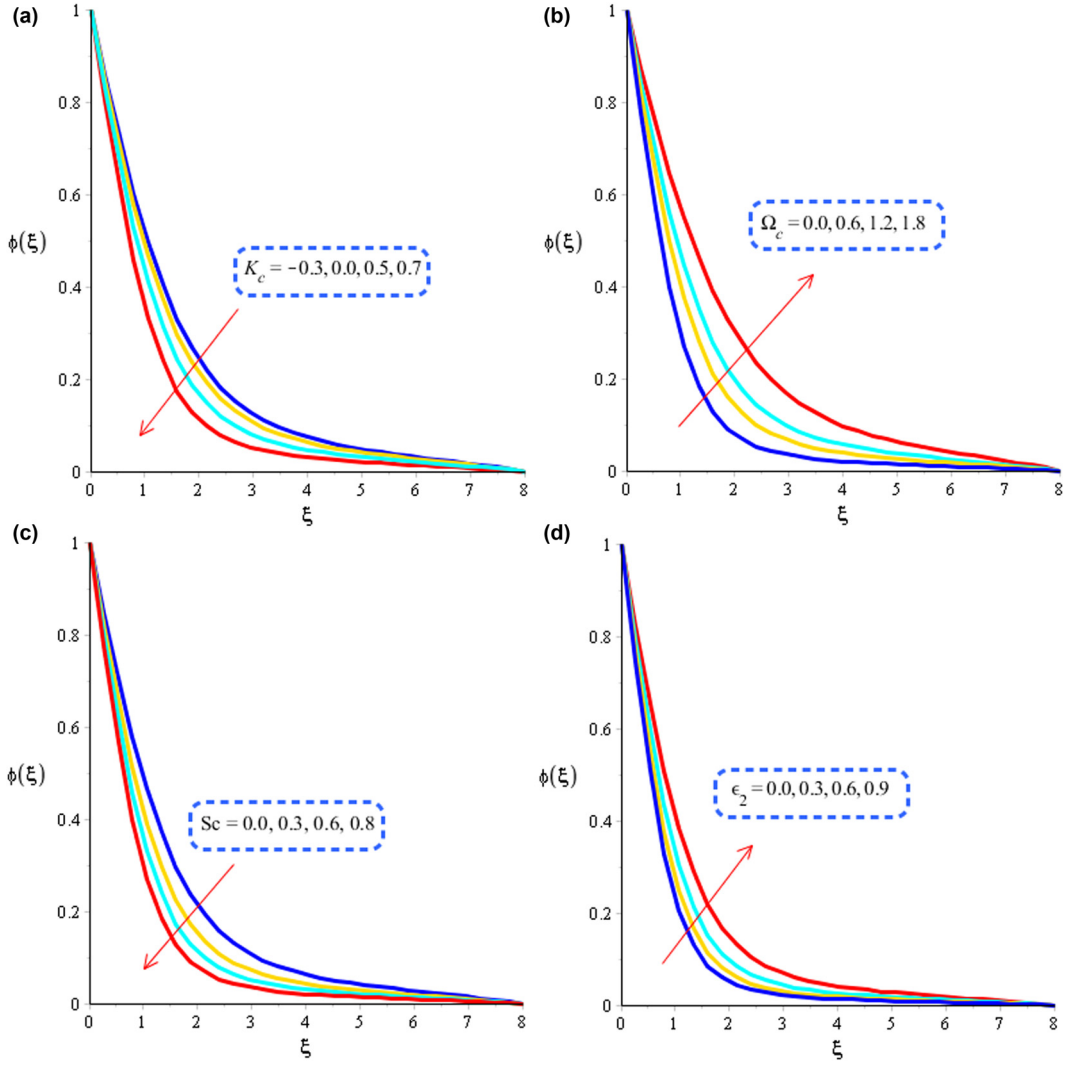

Figure 6: (a) Role of K_c on concentration curves. (b) Role of Sc on concentration curves. (c) Role of Ω_c on concentration curves. (d) Role of ε_2 on concentration curves.

Table 4: Numerical simulations of skin friction coefficient, concentration gradient and temperature gradient *versus* F_r, H_h, Sc, and K_c

		$(\mathbf{Re})^{\frac{1}{m+1}}C_f$	$(\mathbf{Re})^{\frac{-1}{m+1}}\mathbf{Nu}$	$(\mathbf{Re})^{\frac{-1}{m+1}}\mathbf{Sc}$
	0.0	0.9831194688	1.273048742	0.1738269697
F_r	0.3	0.9948702726	1.263799787	0.1636186839
	0.6	1.0055424430	1.244465792	0.1434299640
	−1.5	1.048480792	2.988980397	0.1582282354
H_h	0.3	1.021340103	2.184136239	0.1468662589
	0.7	1.010130191	2.110134671	0.1380771772
	0.0	1.018480792	1.275290361	0.1059774514
Sc	0.3	1.018480792	1.275290361	0.2836633481
	0.6	1.018480792	1.275290361	0.6105156610
	−1.4	1.018480792	1.275290361	0.08312047671
K_c	0.0	1.018480792	1.310199330	0.09127662373
	0.5	1.018480792	1.501284349	0.29611881081

dual trends of K_c is measured by Figure 6a. Two kinds of trend are called destructive and generative chemical reactions for $K_c > 0$ and $K_c < 0$, respectively. It is estimated that the chemical reaction is known as non-reactive reaction for $K_c = 0$. Diffusion into species is decreased *versus* large values of K_c. Further, the generative chemical reaction is higher than the reaction related to destructive and non-reactive reactions. Diffusion into species slows down because chemical reaction among fluid particles occurred. Hence, layers associated with concentration are also reduced when chemical reaction becomes fast among nanoparticles. An influence of Schmidt number (Sc) on concentration curves is addressed by Figure 6b. Diffusion of species slows down with respect to change in Sc. Physically, Sc has inverse proportional *versus* mass diffusivity. Therefore, an inclination into mass diffusion is addressed when mass diffusivity is increased. Hence, a declination role is predicted *versus* impact of Sc. Moreover, concentration layers are inclined with respect to change in Sc. It is the ratio of viscous diffusion and mass diffusion rates. Therefore, mass diffusion rate is decreased *versus* higher impact of Sc. Concentration layers are declined against higher value of Sc. Appearance of Ω_c is noticed on concentration curves plotted by Figure 6c. Three kinds of nanoparticles are inserted into diffusion of species, whereas higher values of Ω_c are observed as a significant performance of species rate. Significant performance of mass species is observed *versus* the role of Ω_c. Figure 6d addresses characterizations of solute particles *versus* the impact of Ω_c Existence of Ω_c is formulated due to the impact of Cattaneo–-Christov theory. A significant achievement into solute particles is observed when Ω_c is enhanced including tri-hybrid nanoparticles.

4.4 Analysis of Sherwood number, temperature gradient, and drag force coefficient

Temperature gradient, Sherwood number, and drag force coefficient are simulated by incorporating influences of Forchheimer number, heat generation number, chemical reaction number, and Sc including the study of ternary hybrid nanoparticles. Impacts related to these parameters on temperature gradient, Sherwood number, and drag force coefficient are simulated as shown in Table 4. Role of F_r boosts surface force but the concentration and temperature gradients are declined when F_r is increased. H_h diminishes the rate of thermal energy, mass diffusion, and surface force. It is estimated that the dual trends (heat absorption and heat generation) are addressed. In both cases for H_h are observed significantly for establish maximum production in rate of concentration and temperature gradients. A declination is predicted in view of surface force *versus* an impact of chemical reaction (generative and destructive) but in terms of Sherwood and Nusselt, numbers are inclined. For the case of Sc, rates of mass diffusion and thermal energy are significantly increased.

5 Conclusion

Solute and thermal characterizations in pseudo-plastic liquid are investigated along with the ternary hybrid nanoparticles. An expanding surface is considered to measure the flow, thermal energy, and solute particles into particles against the distribution of various physical parameters. Darcy's Forchheimer law is incorporated along with non-Fourier's law in the presence of heat generation and heat absorption. A term related to chemical reaction is also considered into solute particles. The finite element approach has used to characterize graphical outcomes. Main findings are addressed below.

- Flow slows down *versus* higher values of Darcy's number, power law number, and Forchheimer number;
- Argumentation is investigated into heat energy of particles for the case of ternary hybrid nanoparticles rather than for case of fluid, nanoparticles, and hybrid nanoparticles.
- Maximum achievement of heat energy for tri-hybrid nanoparticles as compared than nanofluid and hybrid nanoparticles.
- Diffusion of species slows down when Sc is enhanced.
- Applications of ternary hybrid nanoparticles based on present problem are utilized in medicines, cancer cells,

memory devices, materials, electronics, systems, and devices.

Funding information: The authors state no funding involved.

Author contributions: All authors have accepted responsibility for the entire content of this manuscript and approved its submission.

Conflict of interest: The authors state no conflict of interest.

Data availability statement: All data generated or analysed during this study are included in this published article.

References

[1] Koriko OK, Shah NA, Saleem S, Chung JD, Omowaye AJ, Oreyeni T. Exploration of bioconvection flow of MHD thixotropic nanofluid past a vertical surface coexisting with both nanoparticles and gyrotactic microorganisms. Sci Rep. 2021;11(1):1–5.

[2] Ali A, Noreen A, Saleem S, Aljohani AF, Awais M. Heat transfer analysis of Cu–Al_2O_3 hybrid nanofluid with heat flux and viscous dissipation. J Therm Anal Calorim. 2021;143(3):2367–77.

[3] Saleem S, Heidarshenas B. An investigation on energy in a wavy wall microchannel heat sink by using various nanoparticles in fluid flow: two-phase numerical study. J Therm Anal Calorim. 2021;145:1–2.

[4] Pop I, Waini I, Ishak A. MHD stagnation point flow on a shrinking surface with hybrid nanoparticles and melting phenomenon effects. Int J Numer Methods Heat Fluid Flow. 2021. doi: 10.1108/HFF-06-2021-0378.

[5] Tlili I, Samrat SP, Sandeep N, Nabwey HA. Effect of nanoparticle shape on unsteady liquid film flow of MHD Oldroyd-B ferrofluid. Ain Shams Eng J. 2021;12(1):935–41.

[6] Qin Y. Simulation of MHD impact on nanomaterial irreversibility and convective transportation through a chamber. Appl Nanosci. 2021;1–4.

[7] Nawaz M, Madkhali HA, Haneef M, Alharbi SO, Alaoui MK. Numerical study on thermal enhancement in hyperbolic tangent fluid with dust and hybrid nanoparticles. Int Commun Heat Mass Transf. 2021;127:105535.

[8] Nazir U, Abu-Hamdeh NH, Nawaz M, Alharbi SO, Khan W. Numerical study of thermal and mass enhancement in the flow of Carreau-Yasuda fluid with hybrid nanoparticles. Case Stud Therm Eng. 2021;27:101256.

[9] Nazir U, Sohail M, Alrabaiah H, Selim MM, Thounthong P, Park C. Inclusion of hybrid nanoparticles in hyperbolic tangent material to explore thermal transportation *via* finite element approach engaging Cattaneo-Christov heat flux. PLoS one. 2021;16(8):e0256302.

[10] Nazir U, Nawaz M, Alharbi SO. Thermal performance of magnetohydrodynamic complex fluid using nano and hybrid nanoparticles. Phys A: Stat Mech Appl. 2020;553:124345.

[11] Sheikholeslami M, Farshad SA. Investigation of solar collector system with turbulator considering hybrid nanoparticles. Renew Energy. 2021;171:1128–58.

[12] Swain K, Mebarek-Oudina F, Abo-Dahab SM. Influence of MWCNT/Fe_3O_4 hybrid nanoparticles on an exponentially porous shrinking sheet with chemical reaction and slip boundary conditions. J Therm Anal Calorim. 2022;147(2):1561–70.

[13] Faraji H, El Alami M, Arshad A. Investigating the effect of single and hybrid nanoparticles on melting of phase change material in a rectangular enclosure with finite heat source. Int J Energy Res. 2021;45(3):4314–30.

[14] Abdelmalek Z, Nazir U, Nawaz M, Alebraheem J, Elmoasry A. Double diffusion in Carreau liquid suspended with hybrid nanoparticles in the presence of heat generation and chemical reaction. Int Commun Heat Mass Transf. 2020;119:104932.

[15] Nawaz M, Nazir U, Alharbi SO, Alaoui MK. Thermal and solutal analysis in power law fluid under non-Fourier's diffusion conditions. Int Commun Heat Mass Transf. 2021;126:105331.

[16] Latocha J, Wojasiński M, Jurczak K, Gierlotka S, Sobieszuk P, Ciach T. Precipitation of hydroxyapatite nanoparticles in 3D-printed reactors. Chem Eng Processing-Process Intensif. 2018;133:221–33.

[17] Haider I, Nazir U, Nawaz M, Alharbi SO, Khan I. Numerical thermal study on performance of hybrid nano-Williamson fluid with memory effects using novel heat flux model. Case Stud Therm Eng. 2021;26:101070.

[18] Nazir U, Sohail M, Hafeez MB, Krawczuk M, Askar S, Wasif S. An inclination in thermal energy using nanoparticles with casson liquid past an expanding porous surface. Energies. 2021;14(21):7328.

[19] Dadheech PK, Agrawal P, Mebarek-Oudina F, Abu-Hamdeh NH, Sharma A. Comparative heat transfer analysis of MoS2/C2H6O2 and SiO2-MoS2/C2H6O2 nanofluids with natural convection and inclined magnetic field. J Nanofluids. 2020;9(3):161–7.

[20] Shafiq A, Mebarek-Oudina F, Sindhu TN, Abidi A. A study of dual stratification on stagnation point Walters' B nanofluid flow *via* radiative Riga plate: a statistical approach. Eur Phys J Plus. 2021;136(4):1–24.

[21] Marzougui S, Mebarek-Oudina F, Magherbi M, Mchirgui A. Entropy generation and heat transport of Cu–water nanoliquid in porous lid-driven cavity through magnetic field. Int J Numer Methods Heat Fluid Flow. 2021. doi: 10.1108/HFF-06-2021-0378.

[22] Pushpa BV, Sankar M, Mebarek-Oudina F. Buoyant convective flow and heat dissipation of cu–h2o nanoliquids in an annulus through a thin baffle. J Nanofluids. 2021;10(2):292–304.

[23] Dhif K, Mebarek-Oudina F, Chouf S, Vaidya H, Chamkha AJ. Thermal analysis of the solar collector cum storage system using a hybrid-nanofluids. J Nanofluids. 2021;10(4):616–26.

[24] Abdelsalam SI, Zaher AZ. Leveraging elasticity to uncover the role of rabinowitsch suspension through a wavelike conduit: consolidated blood suspension application. Mathematics. 2021;9(16):2008.

[25] Abdelsalam SI, Velasco-Hernández JX, Zaher AZ. Electromagnetically modulated self-propulsion of swimming sperms

via cervical canal. Biomech Modeling Mechanobiol. 2021;20(3):861–78.
[26] Raza R, Mabood F, Naz R, Abdelsalam SI. Thermal transport of radiative Williamson fluid over stretchable curved surface. Therm Sci Eng Prog. 2021;23:100887.
[27] Eldesoky IM, Abdelsalam SI, El-Askary WA, Ahmed MM. The integrated thermal effect in conjunction with slip conditions on peristaltically induced particle-fluid transport in a catheterized pipe. J Porous Media. 2020;23(7):695–713.
[28] Bhatti MM, Abdelsalam SI. Bio-inspired peristaltic propulsion of hybrid nanofluid flow with Tantalum (Ta) and Gold (Au) nanoparticles under magnetic effects. Waves Random Complex Media. 2021;1–26.
[29] Elkoumy SR, Barakat EI, Abdelsalam SI. Hall and transverse magnetic field effects on peristaltic flow of a Maxwell fluid through a porous medium. Glob J Pure Appl Math. 2013;9(2):187–203.
[30] Bhatti MM, Alamri SZ, Ellahi R, Abdelsalam SI. Intra-uterine particle–fluid motion through a compliant asymmetric tapered channel with heat transfer. J Therm Anal Calorim. 2021;144(6):2259–67.
[31] Sohail M, Ali U, Zohra FT, Al-Kouz W, Chu YM, Thounthong P. Utilization of updated version of heat flux model for the radiative flow of a non-Newtonian material under Joule heating: OHAM application. Open Phys. 2021;19(1):100–10.
[32] Wong HF, Sohail M, Siri Z, Noor NF. Numerical solutions for heat transfer of an unsteady cavity with viscous heating. Computers, Mater Continua. 2021;68(1):319–36.
[33] Sakiadis BC. Boundary-layer behavior on continuous solid surfaces: II. The boundary layer on a continuous flat surface. AiChE J. 1961;7(2):221–5.
[34] Fox VG, Erickson LE, Fan LT. Methods for solving the boundary layer equations for moving continuous flat surfaces with suction and injection. AIChE J. 1968;14(5):726–36.
[35] Chen CH. Forced convection over a continuous sheet with suction or injection moving in a flowing fluid. Acta Mechanica. 1999;138(1):1–11.
[36] Nazir U, Saleem S, Nawaz M, Sadiq MA, Alderremy AA. Study of transport phenomenon in Carreau fluid using Cattaneo–Christov heat flux model with temperature dependent diffusion coefficients. Phys A: Stat Mech Appl. 2020;554:123921.